

# FoRA: Low-Rank Adaptation Model beyond Multimodal Siamese Network

Wenyong Xie  
wyxie@xidian.edu.cn  
Xidian University  
Xi'an, Shannxi, China

Yusi Zhang\*  
23011210731@stu.xidian.edu.cn  
Xidian University  
Xi'an, Shannxi, China

Tianlin Hui  
23011210802@stu.xidian.edu.cn  
Xidian University  
Xi'an, Shannxi, China

Jiaqing Zhang  
jqzhang\_2@stu.xidian.edu.cn  
Xidian University  
Xi'an, Shannxi, China

Jie Lei  
jielei@mail.xidian.edu.cn  
Xidian University  
Xi'an, Shannxi, China

Yunsong Li  
ysli@mail.xidian.edu.cn  
Xidian University  
Xi'an, Shannxi, China

## ABSTRACT

Multimodal object detection offers a promising prospect to facilitate robust detection in various visual conditions. However, existing two-stream backbone networks are challenged by complex fusion and substantial parameter increments. This is primarily due to large data distribution biases of multimodal homogeneous information. In this paper, we propose a novel multimodal object detector, named Low-rank Modal Adaptors (LMA) with a shared backbone. The shared parameters enhance the consistency of homogeneous information, while lightweight modal adaptors focus on modality unique features. Furthermore, we design an adaptive rank allocation strategy to adapt to the varying heterogeneity at different feature levels. When applied to two multimodal object detection datasets, experiments validate the effectiveness of our method. Notably, on DroneVehicle, LMA attains a 10.4% accuracy improvement over the state-of-the-art method with a 149M-parameters reduction. The code is available at FoRA.

## CCS CONCEPTS

• Computing methodologies → Object detection.

## KEYWORDS

Multimodal Object Detection, Modal Adaptor, Low-rank Matrix

## 1 INTRODUCTION

Object detection is a crucial task in computer vision as it involves locating and identifying interested objects [8, 9]. During the detection, only considering one modality has limitations, e.g. visible images may not provide sufficient high chromatic contrast and visual fidelity information in poor visual and other increasingly complex conditions [18, 24, 31, 46]. In contrast, infrared images

\*Corresponding author

Permission to make digital or hard copies of all or part of this work for personal or classroom use is granted without fee provided that copies are not made or distributed for profit or commercial advantage and that copies bear this notice and the full citation on the first page. Copyrights for components of this work owned by others than the author(s) must be honored. Abstracting with credit is permitted. To copy otherwise, or republish, to post on servers or to redistribute to lists, requires prior specific permission and/or a fee. Request permissions from permissions@acm.org.

ACM MM, 2024, Melbourne, Australia

© 2024 Copyright held by the owner/author(s). Publication rights licensed to ACM.

ACM ISBN 978-x-xxxx-xxxx-x/YY/MM

<https://doi.org/10.1145/nnnnnnn.nnnnnnn>

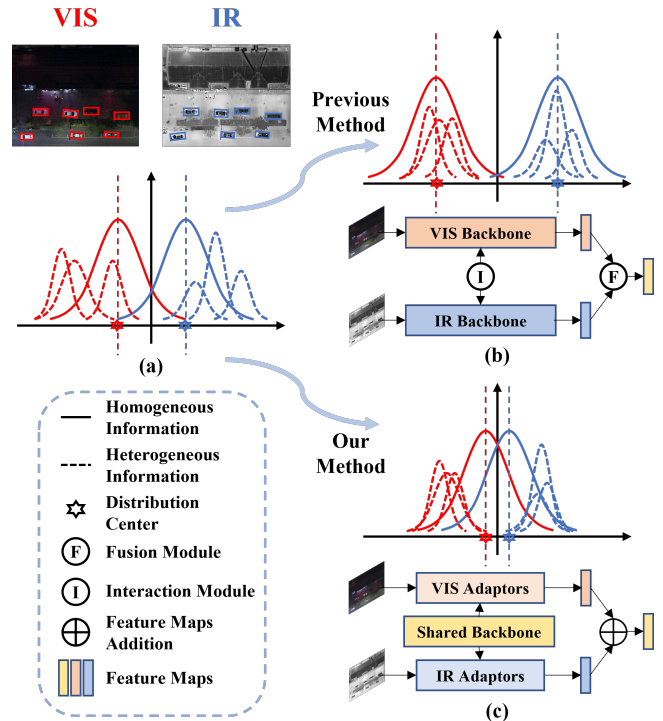


**Figure 1: Illustrations of changes in statistical data distributions for valid information and corresponding multimodal object detection structures. (a) Valid information (homogeneous information and heterogeneous information) exhibits different distribution biases in multimodal images. (b) Previous methods employ two-stream backbone (bottom) to extract features, bringing larger distribution biases. (c) We greatly reduce the biases and model scale by combining shared backbone and modal adaptors (bottom).**

[17, 19] reflect the surface temperature of objects with temperatures above absolute zero. And they exhibit highlighted contrast information and sharp edge contours, which are less susceptible to changes in visual conditions [27].

In this case, the assistance of combining visible and infrared images can gain deep insights into multimodal object detection

(MOD) to maximize their respective strengths through modality cooperation [38, 39, 51, 52]. A direct way to perform MOD with deep neural networks (DNNs) is to build a symmetric two-stream backbone where features are extracted independently from each modality. And then these independent multimodal features are fused to complete and enhance the detection performance [5, 38], as shown in Figure 1 (b).

Such an independent two-stream backbone is inadequate due to distribution biases of multimodalities, thus resulting in suboptimal solutions. On the one hand, the two modalities (visible and infrared images) have not been learned together making biases of multimodal features larger. Therefore, well-designed fusion and interaction strategies are needed to retain the consistency of homogeneous information, such as Cross-modal Conflict rectification module (CCR) in [15], Differential Modality Aware Fusion module (DFMA) in [58], and Inter-modality Cross-Attention module (ICA) in [50]. On the other hand, significant and substantial increases in the parameters of additional backbone and fusion module are observed when integrating the unimodal model. For instance, YOLOv8l [23] (44.48M) requires at least one backbone for each additional modality, which results in a parameter increase of 19.78M (44.47%).

In this paper, we propose a novel multimodal object detector named Low-rank Modal Adaptor (LMA) to address distribution biases of multimodalities while emphasizing lightweight. Different from the previous methods which extract multimodal respective information with **completely independent network parameters**, LMA introduces **identical network parameters to extract homogeneous information and distinct parameters to focus on heterogeneous information**. Concretely, we employ a shared backbone to extract the modality-shared features while lightweight modal adaptors for characteristics unique to each modality. Due to the shared parameters, the identification of objects is more uniform because the data distribution bias of homo-information is greatly reduced as illustrated in Figure 1, thus avoiding complex design of fusion and interaction modules. Considering that varying heterogeneity in multimodal features at different network levels seriously affects the choice of parameter counts in adaptors, we employ singular value decomposition (SVD)-like low-rank matrices as our adaptors and design an importance-aware training strategy to dynamically allocate the matrix ranks. Note that adaptors with low-rank matrices own few parameters, which means the network solely introduces little computational overhead for each additional modality. Our contributions can be summarized as follows:

- We propose a novel detector named LMA to tackle the issue of large data distribution bias between two modalities. To our best knowledge, our structure is the first work that combines a shared backbone and lightweight modal adaptors for multimodalities, enabling more effective extraction of both homogeneous and heterogeneous information.
- To meet the demand for varying parameter counts of adaptors across different multimodal feature levels, we design an adaptive matrix rank allocation strategy that incorporates joint gradients and singular values as importance metric.
- We conduct experiments on two multimodal object detection benchmarks: DroneVehicle [46] and LLVIP [20]. We prove the large data distribution bias of multimodal features and

the varying heterogeneity of different feature levels in two-stream backbone networks. Moreover, our method achieves SOTA and a 10.4% increase in accuracy over previous methods with a 1000× reduction in parameter incremental percentages on DroneVehicle dataset.

## 2 RELATED WORKS

### 2.1 Visible Object Detection

**Object Detection** on visible images is a pivotal and extensively utilized task in computer vision. With the publication of numerous benchmark datasets such as Pascal VOC [11], ADE20K [57] and COCO-Stuff [2], object detectors based on deep neural network have been extensively researched. The detection models can be roughly divided into single-stage detectors and two-stage detectors. Two-stage detectors, such as Fast R-CNN [13], Faster R-CNN [43], can achieve high precision through coarse localization and fine feature extraction of region of interest (RoI), while the model sizes are generally large. In contrast, the structure of the single-stage detectors, such as RetinaNet [30], SSD [33] and YOLO-series detectors [1, 6, 7, 12, 22, 40–42], are more lightweight but less accurate. In these methods, Convolutional Neural Networks (CNN) are typically used to construct the backbones. Among various object detection algorithms, single-stage detector YOLOv8 [23] strikes an excellent balance between accuracy and the count of model parameters. Therefore, we have chosen it as our unimodal model.

**Oriented Object Detection** refers to using rotated bounding boxes to represent detection results, which can provide more accurate location of objects. Detectors based on horizontal bounding box are plagued by multiple objects of interest in one anchor. Therefore, many researches about oriented object detection [10, 21, 34, 45, 60] have been presented to alleviate this problem. Oriented R-CNN [48] adjusts receptive fields of neurons in accordance with object shapes and orientations. S2Anet [14] adopts alignments between horizontal receptive fields and rotated anchors to get a better feature representation. In this paper, we replace the detection head of YOLOv8 with an oriented bounding box (OBB) detection head to construct an oriented object detector.

### 2.2 Multimodal Object Detection

Multimodal object detection based on visible-infrared image pairs has become a promising research field to address the issue that visible images are insufficient for capturing crucial information in poor visual conditions [35, 36, 59]. Current multimodal object detection algorithms concentrate on two primary concerns: (1) how to extract valid information of each modality? and (2) how to effectively fuse the multimodal features to generate fusion features that contain distinct object features and complementary information from both modalities? Zhao *et al.* [56] coarsely remove interfering information within each modality and design a dynamic feature selection module to finely select desired features for feature fusion. He *et al.* [15] exam contextual information of analogous pixels to alleviate multimodal information with semantic conflicts, and then fuse multimodal features by assessing intra-modal importance to select semantically rich features and mining inter-modal complementary information. Chen *et al.* [5] emphasize object region

while aligning the object regions and utilize a channel-wise attention mechanism with illumination guidance to eliminate the imbalance between different modalities. Zhou *et al.* [58] design a novel Differential Modality Aware Fusion (DMAF) module to make two modalities complement each other and align them adaptively through an illumination aware feature alignment module.

Nonetheless, the aforementioned methods employ two-stream backbone networks to extract features of each modality. To ensure consistency of modality-shared features and heterogeneity of modality-unique features, complex feature interaction and fusion modules have been designed within the backbones. This is challenging in terms of model design and introduces a significant number of additional parameters based on unimodal models. To address this problem, we propose LMA, which utilizes lightweight model structures to enhance the consistency of homogeneous information while preserving heterogeneous information.

### 3 METHOD

In this section, we firstly introduce a general formulation of multimodal object detection and point out the limitations of symmetric two-stream backbone networks. Secondly, we detail our detector combining a shared backbone with modal adaptors. We demonstrate the validity of this structure through formulas. Lastly, as our method involves the choices of adaptor parameter counts, we introduce an importance-aware adaptive rank allocation strategy to control the parameter budget.

#### 3.1 MOD Formulation

**3.1.1 Formulation of MOD.** As shown in Figure 1 (a), assume the distribution of each valid information in multimodal images is Gaussian Distribution with a mean  $\mu$  and a variance  $\sigma^2$ , denoted as  $X \sim N(\mu, \sigma^2)$ . The data distribution of every visible-infrared image pair can be represented as follows:

$$D_{mod} \sim C_{mod} N(\mu_{mod}, \sigma_{mod}^2) + \sum_{i=1}^{n_{mod}} C_i N(\mu_i, \sigma_i^2), \quad (1)$$

$$mod = \{v, t\},$$

where the subscripts  $v$  and  $t$  refer to the visible and infrared modality respectively.  $C_{mod}$  denotes the intensities of homogeneous information in each modality, while  $\mu_{mod}$  and  $\sigma_{mod}^2$  are their corresponding mean and variance. Similarly,  $C_i$  and  $\mu_i, \sigma_i^2$  for  $i = 1, \dots, n_{mod}$  represent the intensities of unique information in each modality and their data distribution properties.

In the multimodal object detection, it is desired to generate features that maintain consistency of homogeneous information while minimizing loss of modality-unique information as possible. Therefore, fusion feature maps with ideal data distribution can be represented as follows:

$$D_f \sim (C_v + C_t) N(\mu_f, \sigma_f^2) + \sum_{i=1}^{n_v+n_t} C_i N(\mu_i, \sigma_i^2), \quad (2)$$

$$s.t. \frac{1}{n_v + n_t} \sum_{i=1}^{n_v+n_t} \mu_i \approx \mu_f,$$

where the merged distribution sums the original intensities of the homogeneous information and generates a new distribution

$N(\mu_f, \sigma_f^2)$ . Meanwhile, all heterogeneous information intensities are preserved to leverage multimodal complementary information. Ideally, the geometric center of their means is approximated as the mean of the homogeneous information, as shown in Formula (2).

**3.1.2 Two-stream Backbone Networks.** Deep neural networks (DNN) can be viewed as functions with learnable parameters that maps input data to a high-dimensional feature space. Therefore, the process of feature extraction in two-stream backbone networks can be represented as follows:

$$E_{mod} = B(D_{mod}; \omega_{mod})$$

$$\sim C_{mod}^* N(\mu_{mod}^*, \sigma_{mod}^{*2}) + \sum_{i=1}^{n_{mod}} C_i^* N(\mu_i^*, \sigma_i^{*2}), \quad (3)$$

$$\frac{1}{n_{mod}} \sum_{i=1}^{n_{mod}} \mu_i^* \approx \mu_r^*.$$

Here,  $E$  is the data distribution of modality features and  $B$  denotes the mapping function of the backbone with parameters  $\omega_{mod}$ . The distribution of input data significantly impacts the training and formation of parameters. In turn, a backbone with specific parameters maps the inputs to corresponding data space. As illustrated in Formula (3) and Figure 1 (b), multimodal features extracted by two-stream backbone will form respective new geometric center  $\mu_{mod}^*$ . This will significantly large the biases of homogeneous information and we prove it in subsequent experiments (as illustrated in Figure 5):

$$|\mu_v^* - \mu_t^*| > |\mu_v - \mu_t|. \quad (4)$$

To obtain the ideal fusion features as shown Formula (2) from Formula (3), it is necessary to design efficient fusion functions, which are generally complex and sometimes lack generalization to various datasets. Moreover, two-stream backbones employs completely independent parameters  $\omega_v$  and  $\omega_t$  to extract homogeneous information. Such structures are empirically parameter redundant.

#### 3.2 Proposed Detector LMA

**3.2.1 Overview of the Framework.** The overall architecture of the proposed method is shown in Figure 2. The LMA extends a unimodal model and attaches two lightweight modal adaptors to all feature extraction layers, such as Convolutional, Transformer [47], and Fully Connected layers [28], of the backbone. Adaptor parameters can be merged with corresponding backbone layer to form a new feature extraction layer with the same shape. Details of modal adaptors are introduced in Section 3.2.2.

The parameters of the shared backbone, visible adaptors and infrared adaptors are denoted as  $\omega_{shared}$ ,  $\omega_{vada}$  and  $\omega_{tada}$  respectively. When a modality data is received, a new backbone layer is created by merging shared layer and corresponding modal adaptor to extract modality features, which can be represented as follows:

$$E_v = B(D_v; \omega_{vada} + \omega_{shared}), \quad E_t = B(D_t; \omega_{tada} + \omega_{shared}), \quad (5)$$

where shared backbone parameters  $\omega_{shared}$  are influenced by both modalities. When acting in turn on multimodal data, they thus tend to map homogeneous information in different modality to the same feature space. The modal adaptors then focus more on the

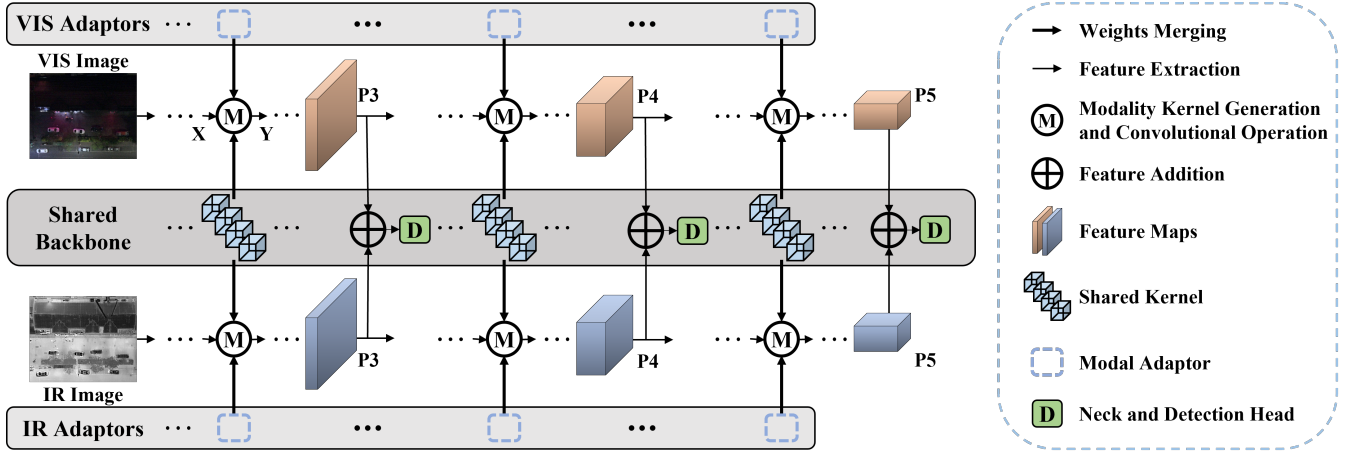


**Figure 2: Overview of LMA (Taking convolutional backbone as an example).** When a convolutional layer works, a new modality convolutional kernel is first generated by merging the modal adaptor weights and the shared convolutional kernel weights. Then the input data are convolved with the new modality kernel to output the extracted feature map. The details of this process are shown in Figure 3 and Figure 4. “P3”, “P4” and “P5” represent the features need to be fused and then fed into detector.

remaining heterogeneous information:

$$E_{mod} \sim C'_{mod} N(\mu'_{mod}, \sigma'^2) + \sum_{i=1}^{n_{mod}} C'_i N(\mu'_i, \sigma'^2_i), \quad (6)$$

$$|\mu'_v - \mu'_t| \ll |\mu_v^* - \mu_t^*|. \quad (7)$$

Formulas (6)-(7) demonstrate that the shared parameter structure effectively reduces distribution biases in homogeneous information during feature extraction, as shown in Figure 1 (c). We also experimentally prove this in subsequent experiments that illustrated in Figure 5. Based on Formulas (6)-(7), we can obtain the ideal fusion features data distribution approximating that in Formula (2) through simple addition operation. The method thus gets rid of designs of complex feature fusion mapping functions and enhances robustness of the model.

In terms of model scale, the lightweight adaptors introduce only a small increase in parameters to the unimodal model:

$$S(\omega_v) = S(\omega_t) = S(\omega_{shared}), \quad (8)$$

$$\text{and } S(\omega_{vada}) = S(\omega_{tada}) \ll S(\omega_{shared}), \quad (9)$$

$$\text{so } S(LMA) = S(\omega_{vada}) + S(\omega_{tada}) + S(\omega_{shared}) \ll S(\omega_v) + S(\omega_t) = S(\text{two-stream backbone}), \quad (10)$$

where  $S(\cdot)$  denotes the count of parameters. Formula (10) means that our method greatly reduces parameter redundancy in multi-modal models. In this case, if a new modality  $m$  needs to be added, only  $S(\omega_{mada})$  will be introduced to the original model. This is a little addition compared to the computational overhead of the entire model.

**3.2.2 Modal Adaptor.** As mentioned in Section 3.2.1, modal adaptors should be lightweight compared to the entire modal and its parameters could be merged with the feature extraction layers of the backbone. Inspired by [16] and [54], we apply SVD-like low-rank matrices as modal adaptors. Concretely, taking a convolutional layer of the backbone as an example, the weight parameter, denoted by  $\mathcal{K}_{shared} \in \mathbb{R}^{C1 \times C2 \times K \times K}$ , is a 4-dimensional tensor, where  $K$

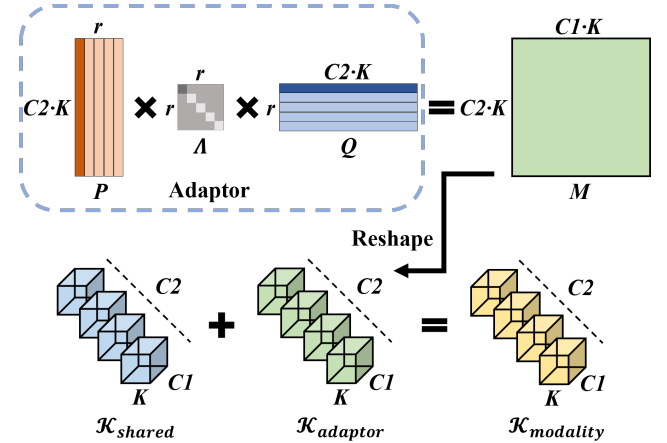


**Figure 3: Details of adaptor structure and merge process of parameters (convolutional layer for example).** Adaptors comprise three low-rank matrices  $P$ ,  $\Lambda$ ,  $Q$ , which generate the adaptor kernel by matrix multiplication and reshaping. Weights of modality kernel are derived from the sum of the shared layer weights and the adaptor kernel weights.

represent the width and height of the spatial window of the convolutional kernel, while  $C1$  and  $C2$  denote the number of input channels of the input to the layer and the number of kernels learned in the layer, respectively. As shown in Figure 3, the adaptor of this layer comprises three low-rank matrices that are multiplied to obtain the adaptor parameter matrix  $M$ :

$$M = PAQ, \quad (11)$$

where  $P \in \mathbb{R}^{C2 \times K \times r}$  and  $Q \in \mathbb{R}^{r \times C1 \times K}$  represent the lift and right singular vectors of  $M \in \mathbb{R}^{C2 \times K \times C1 \times K}$  and the diagonal matrix  $\Lambda \in$

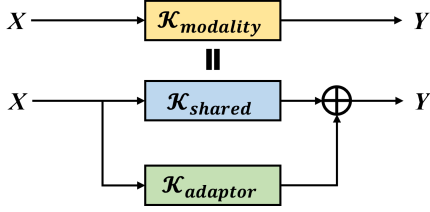


**Figure 4: The equivalent data flow process for convolution of input data  $X$  and  $\mathcal{K}_{modality}$ .  $X$  convolves with  $\mathcal{K}_{shared}$  (top branch) and  $\mathcal{K}_{adaptor}$  (bottom branch) and results in output  $Y$  after summation.**

$\mathbb{R}^{r \times r}$  contains the singular values  $\{\lambda_i\}_{1 \leq i \leq r}$  with inner rank:

$$r \ll \min(C1 \cdot K, C2 \cdot K). \quad (12)$$

We further denote  $\mathcal{G}_i = \{P_i, \lambda_i, Q_i\}$  as triplet containing the  $i$ -th singular value and vectors (as shown in Figure 3, the dark part of  $P$ ,  $\Lambda$ ,  $Q$  represents a triplet). In practice, since  $\Lambda$  is diagonal, we only need to save it as a vector in  $\mathbb{R}^r$ .

To merge parameters of shared backbone layer and adaptor, we reshape the adaptor matrix to an adaptor convolution kernel  $\mathcal{K}_{adaptor} \in \mathbb{R}^{C1 \times C2 \times K \times K}$  with the same shape as  $\mathcal{K}_{shared}$ :

$$\mathcal{K}_{modality} = \mathcal{K}_{shared} + \mathcal{K}_{adaptor}, \quad (13)$$

subsequently, the convolutional kernel  $\mathcal{K}_{modality} \in \mathbb{R}^{C1 \times C2 \times K \times K}$  for modal feature extraction is obtained by adding the weights of shared kernel and the adaptor kernel. Following basic theory of convolution [26], modality kernel is equal to the parallel architectural branches illustrated in Figure 4, which enables the layer to focus on different types of information in the input data simultaneously. In addition to convolution layers, adaptor parameter matrices can be reshaped to the shape of various common feature extraction structures. Our method thus could be generalized to any models with common layers.

The calculations of parameter counts for the adaptor and the convolutional layer are as follows:

$$\begin{aligned} S(adaptor) &= S(P) + S(\Lambda) + S(Q) \\ &= C2 \cdot K \cdot r + r \cdot C1 \cdot K + r \\ &= r(K(C1 + C2) + 1), \end{aligned} \quad (14)$$

$$S(\mathcal{K}_{shared}) = C1 \cdot C2 \cdot K \cdot K, \quad (15)$$

$$S(adaptor) \leq S(\mathcal{K}_{shared}), \quad (16)$$

$$\text{when } r \leq \frac{C1 \cdot C2 \cdot K \cdot K}{K(C1 + C2) + 1} \approx \frac{C1 \cdot C2 \cdot K}{C1 + C2}. \quad (17)$$

Based on Formula (12) and Formulas (14)-(17), Formula (9) could be easily satisfied.

### 3.3 Adaptive Rank Allocation Strategy

As mentioned in Section 3.2.1, adaptors are designed for heterogeneous information. In DNNs, shallow features primarily contain detailed information such as texture and contours of images, while deep features mainly include the semantic information of the objects. Therefore, the amount of heterogeneous information in features maps between modalities varies with feature levels. We prove this in subsequent experiments as shown in Figure 7. The

importance of adaptor matrices thus varies significantly across blocks and layers. Adding more trainable parameters to the critical adaptor matrices can lead to better model performance. In contrast, adding more parameters to those less important matrices yields marginal gains or even hurts model performance. The parameters of the adaptor depend on the inner rank, which is the number of triplets  $\mathcal{G}_i$  in the SVD matrix. Setting ranks evenly to all adaptor matrices/layers thus often leads to suboptimal performance.

To address this problem, we propose a training strategy to adaptively allocate rank of adaptor based on importance of SVD matrix triplets under limited parameter budget. We define parameter budget  $b^{(it)}$  as the total inner rank of all adaptors, where  $it = 0, \dots, T$  represents the index of training step. We set the initial rank of each adaptor as  $r = b^{(0)}/n$ , where  $n$  is the number of adaptors and gradually reduce  $b^{(it)}$  to target budget  $b^{(T)}$  during training. We iteratively prune singular values by setting the singular value in triplet of low importance to zero, which will discard the entire triplet, to achieve corresponding budget.

For clear reference, we use  $k$  to index the adaptor, i.e.,  $M_k = P_k \Lambda_k Q_k$  for  $k = 1, \dots, n$  and denote the  $i$ -th triplet of  $M_k$  as  $\mathcal{G}_{k,i} = \{P_{k,*i}, \Lambda_{k,i}, Q_{k,i*}\}$  and its importance score as  $IS_{k,i}$ . Previous methods [3, 25] apply the magnitude of singular values to quantify the importance of every triplet or use the gradient values of the training loss to quantify the importance of every parameter [29, 37, 44, 55]. We combine the both metrics to determine the basic importance  $I(\cdot)$  of each entry in the adaptor triplets:

$$I(P_{k,ij}) = I(Q_{k,ij}) = I(\omega_{k,ij}) = |\nabla_{\omega_{k,ij}} \mathcal{L}(P, \Lambda, Q)|, \quad (18)$$

$$I(\Lambda_{k,i}) = |\Lambda_{k,i} \cdot \nabla_{\Lambda_{k,i}} \mathcal{L}(P, \Lambda, Q)|, \quad (19)$$

where  $\omega_{k,ij}$  is any trainable parameter in left and right singular vectors.  $\mathcal{L}(\cdot)$  is the loss of the task, which contains categorical loss and regression loss in object detection, and  $\nabla$  denotes the gradient operation. Here, importance of singular vectors is determined only by gradients of loss, while that of singular values is quantified by the magnitude of gradient-weight product. However, such a score in Equations (18)-(19) is estimated on the sampled mini batch. The stochastic sampling and complicated training dynamics incur high variability and large uncertainty for estimating the importance. Therefore, we utilize the importance smoothing and uncertainty quantification in [55] to resolve this issue:

$$\bar{I}^{(it)} = \beta_1 \bar{I}^{(it-1)} + (1 - \beta_1) I^{(it)}, \quad (20)$$

$$\bar{U}^{(it)} = \beta_2 \bar{U}^{(it-1)} + (1 - \beta_2) |I^{(it)} - \bar{I}^{(it)}|, \quad (21)$$

where  $0 < \beta_1, \beta_2 < 1$ .  $\bar{I}^{(it)}$  is the smoothed importance by exponential moving average and  $\bar{U}^{(it)}$  is the uncertainty term quantified by the local variation between  $I^{(it)}$  and  $\bar{I}^{(it)}$ . Then the importance score of each entry is defined as the product between  $\bar{I}^{(it)}$  and  $\bar{U}^{(it)}$  and denoted as  $s(\cdot)$ :

$$s^{(it)} = \bar{I}^{(it)} \cdot \bar{U}^{(it)}. \quad (22)$$

The importance score of  $i$ -th triplet of  $M_k$  can be represented as:

$$IS_{k,i} = s(\Lambda_{k,i}) + \frac{1}{C2 \cdot K} \sum_{j=1}^{C2 \cdot K} s(P_{k,ji}) + \frac{1}{C1 \cdot K} \sum_{j=1}^{C1 \cdot K} s(Q_{k,ij}), \quad (23)$$

where we employ the mean importance of  $P_{k,*i}$  and  $Q_{k,i*}$  as its importance score such that  $IS_{k,i}$  does not scale with the number of parameters in triplet.

All trainable parameters of adaptors can be denoted as  $P = \{P_k\}_{k=1}^n$ ,  $\Lambda = \{\Lambda_k\}_{k=1}^n$  and  $Q = \{Q_k\}_{k=1}^n$ . At the  $i$ -th step, we first update the trainable parameter by gradient descent:

$$P_k^{(it+1)} = P_k^{(it)} - \eta \nabla_{P_k} \mathcal{L}(P, \Lambda, Q); \quad (24)$$

$$Q_k^{(it+1)} = Q_k^{(it)} - \eta \nabla_{Q_k} \mathcal{L}(P, \Lambda, Q),$$

$$\tilde{\Lambda}_k^{(it)} = \Lambda_k^{(it)} - \eta \nabla_{\Lambda_k} \mathcal{L}(P, \Lambda, Q), \quad (25)$$

where  $\eta > 0$  is learning rate. Then, given importance score of triplet set  $IS_k^{(it)}$  that contains all adaptor matrices, the singular values are pruned following:

$$\Lambda_k^{(it+1)} = \begin{cases} \tilde{\Lambda}_{k,i}^{(it)}, & \text{if } IS_{k,i}^{(it)} \text{ is in the } top - b^{(it)} \text{ of } IS_k^{(it)} \\ 0, & \text{otherwise} \end{cases}. \quad (26)$$

In this way, we adaptively allocate higher rank to more important adaptors under a limited parameter budget.

## 4 EXPERIMENTS

### 4.1 Dataset and Evaluation Metrics

**DroneVehicle Dataset** [46] is a large-scale drone-based visible-infrared dataset that contains 953,087 vehicle instances in 56,878 images with oriented bounding boxes for five categories (car, bus, truck, van and freight car). The dataset is collected using drone platform under different scenes and lighting conditions. The whole dataset is split into a training set, a validation set and a test set.

**LLVIP Dataset** [20] is a very recently released visible-infrared paired pedestrians dataset which is collected in low-light environments. And most of the images were captured in very dark scenes. The dataset contains 16,836 image pairs with horizontal boxes for one category (person).

**Evaluation Metrics.** We employ the COCO-style metric of the mean average precision (mAP) to assess the accuracy of MOD. For mAP, an Intersection over Union (IoU) threshold such as 0.5 (denoted as mAP@0.5), 0.5-0.95 (denoted as mAP) is used to calculate True Positives (TP) and False Positives (FP). Meanwhile, we utilize the parameter counts (Megabyte, denoted as M) to characterize the size of models, along with its computational and storage overheads.

### 4.2 Implementation Details

We select YOLOv8l as the unimodal model. We use oriented detection head for DroneVehicle dataset while horizontal detection head for LLVIP. All detectors are trained for 50 epochs with a batch size of 8 on an NVIDIA A100-SXM-80GB GPU. We optimize the training process using Adam algorithm. The input image size is set to  $640 \times 640$ . We set the initial average rank to 9 and the target average rank to 6. We warm up the training for 8 epochs, where the rank budget remains constant, and then follow a cubic schedule to decrease the budget until it reaches target budget in the 25-th epoch. After that, we fix the rank allocation and train the model for last 25 epochs. All experiments are conducted based on the modified code library Ultralytics [23] and all other hyperparameters is the same as its default settings.

### 4.3 Comparison with State-of-the-Art Methods

**Comparison of Accuracy on DroneVehicle.** We compare unimodal models and our LMA with the recent state-of-the-art methods on the val set of the DroneVehicle (shown in Table 1). Among the single-modal methods, the YOLOv8l outperforms all single-modal detectors in both modalities. Detection with infrared modality generally performs better than detection with visible modality. The YOLOv8l exhibits lower accuracy in detecting ‘Truck’ in infrared images compared to visible images, while the opposite is true for ‘Freight Car’. Among the multi-modal methods, our method utilizes the complementary information from both modalities and achieve the highest accuracy in three categories – ‘Car’, ‘Truck’ and ‘Freight Car’. Multimodal detector LMA achieves a 4.4% mAP@0.5 higher than the unimodal model. In addition, **LMA outperforms the current state-of-the-art method by 10.4% in mAP@0.5!**

**Comparison of Accuracy on LLVIP.** As shown in Table 2, our proposed method is compared with several state-of-the-art detectors namely Cascade R-CNN [4], CFT [38] and CALNet [15]. LMA achieves promising performance on this dataset, outperforming the highest accuracy among all methods by 1.8% mAP. The superior performance on both multimodal object detection datasets demonstrates the effectiveness and robustness of LMA.

**Comparison of Network Parameters.** As shown in Table 3, previous methods would introduce over 50% of the parameter counts to adapt the inputs of two modalities based on unimodal models. Otherwise, the unimodal models are already of large size. Moreover, if there are complex fusion or interaction modules in multimodal detectors, the parameter increments would reach more than three times of the original models. Among the five methods, **LMA is the smallest detector with only a 0.34% parameter increment.** We reduce the parameter increment by approximately 1000× compared to the state-of-the-art method while still achieving the best performance. This demonstrates the effectiveness of our method in reducing parameter redundancy.

### 4.4 Ablation Studies

Ablation experiments are conducted on the DroneVehicle val set. We introduce the Pearson product-moment correlation coefficient ( $|\rho|$ ) between two modality feature maps to represent the biases of the multimodal information data distribution.

**Ablation on the Structure of LMA.** The baseline is a two-stream backbone detector based on YOLOv8l and fused by addition. We calculate the Pearson product-moment correlation coefficient between two modality feature maps of multimodal detectors in the stages that correspond to the P3, P4, P5 in YOLOv8l. For LMA, the modal kernels are split into shared kernels and adaptor kernels as shown in Figure 4 to extract the homogenous information and heterogeneous information separately. We thus calculate the distribution biases of features generated by both shared backbone and modal adaptors. The statistics are made on the correlation coefficients  $|\rho|$  between two modalities and illustrate the proportion of different correlation coefficients  $|\rho|$  (0.0 ~ 1.0) as a line chart in Figure 5. There is a significant bias between the data distributions of all the multimodal information extracted by two-stream backbone networks. In contrast, LMA utilizes a shared backbone to enhance the consistency of homogeneous information while preserving the



**Table 1: Detection results (mAP@0.5, in %) on DroneVehicle val dataset. "Unimodal Model" represents the base unimodal model of the multimodal detector, the same is true in Table 2 and Table 3. Note that all detectors locate and classify vehicles with OBB (Oriented Bounding Box) heads. Best results highlighted in BOLD.**

Detectors	Unimodal Model	Car	Truck	Freight Car	Bus	Van	mAP@0.5	Modal
RetinaNet [30]	-	78.5	34.4	24.1	69.8	28.8	47.1	Visible
Faster R-CNN [43]	-	79.7	42.0	34.0	76.9	37.7	54.1	
S2ANet [14]	-	79.9	50.0	36.2	82.8	37.5	57.3	
Oriented R-CNN [48]	-	80.3	55.4	42.1	86.8	46.9	62.3	
YOLOv8l [23]	-	97.3	81.4	65.1	97.3	68.1	81.8	
RetinaNet [30]	-	88.8	35.4	39.5	76.5	32.1	54.5	Infrared
Faster R-CNN [43]	-	89.7	41.0	43.1	86.3	41.2	60.3	
S2ANet [14]	-	89.7	51.0	50.3	89.0	44.0	64.8	
Oriented R-CNN [48]	-	89.6	53.9	53.9	89.2	41.0	65.5	
YOLOv8l [23]	-	98.5	69.5	73.8	<b>98.0</b>	<b>72.0</b>	82.4	
Halfway Fusion [32]	Faster R-CNN	89.9	60.3	55.5	89.0	46.3	68.2	Visible+Infrared
AR-CNN [53]	Faster R-CNN	90.1	64.8	62.1	89.4	51.5	71.6	
TSFADet [49]	Oriented R-CNN	89.9	67.9	63.7	89.8	54.0	73.1	
CALNet [15]	ResNet50	90.1	70.7	67.5	89.7	55.0	74.6	
CALNet [15]	YOLOv5l	90.3	73.7	68.7	89.7	59.7	76.4	
<b>LMA</b>	YOLOv8l	<b>98.7</b>	<b>85.5</b>	<b>81.2</b>	96.8	71.7	<b>86.8</b>	

**Table 2: Detection results (mAP, in %) on LLVIP dataset. All methods detect with visible modality and Infrared modality. Best results highlighted in BOLD.**

Detectors	Unimodal Model	mAP
Faster R-CNN [43]	Faster R-CNN	56.9
RetinaNet [30]	RetinaNet	56.9
Cascade R-CNN [4]	Cascade R-CNN	59.6
CFT [38]	YOLOv5l	63.6
CALNet [15]	ResNet50	63.4
CALNet [15]	YOLOv5l	63.9
<b>LMA</b>	YOLOv8l	<b>65.7</b>

**Table 3: Parameter analysis of detectors. "Param Increment" demonstrates the incremental parameters of multimodal object detectors based on the unimodal models.**

Detectors	Params (M)	Unimodal Params (M)	Param Increment
Halfway Fusion	144.86	129.62	11.76%(15.24M)
Faster R-CNN	64.81	41.53	56.06%(23.28M)
CFT	206.03	47.05	337.90%(158.98M)
CALNet	193.64	47.05	311.56%(146.59M)
<b>LMA</b>	<b>44.63</b>	<b>44.48</b>	<b>0.34%(0.15M)</b>

high variability of multimodal heterogeneous information using modal adaptors.

We compare the accuracy performance and parameters of LMA with the baseline as shown in Table 4. LMA achieves a 1.7% mAP@0.5

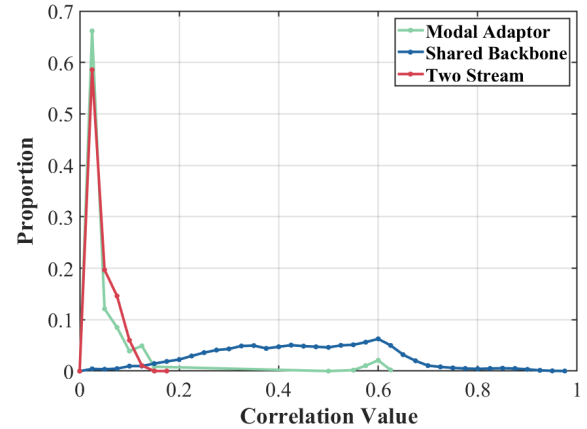


**Figure 5: The data distribution biases (Pearson product-moment correlation coefficient ( $|\rho|$ )) between two modality feature maps. The red line represents the baseline feature maps. The green and blue lines represent feature maps extracted by adaptor kernels and shared kernels respectively.**

improvement in accuracy while reducing parameter increment by a factor of 130, which means we could introduce other modalities with little concern for parameter limitations. Figure 6 presents the visualization results of LMA. In two-stream backbone networks, the data distributions of objects and background information in each modality tend to be similar due to the complete independence of feature extraction. In addition, the difference of data distribution between modalities exacerbates the issue that object features in fusion feature maps are obscured in a large amount of background

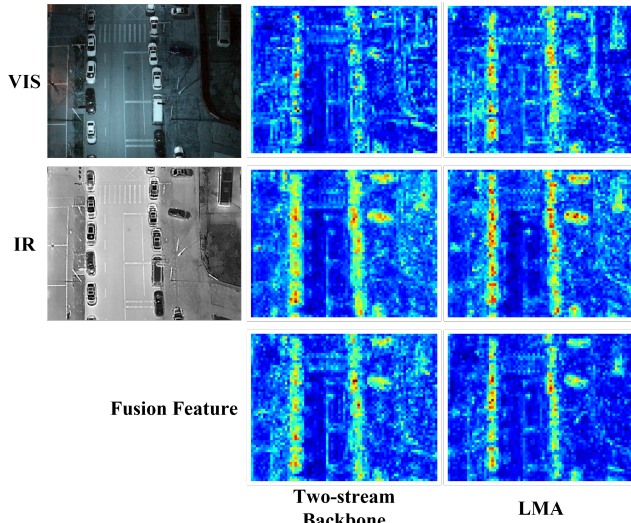


Figure 6: Visualization of feature maps in P3 of LMA and two-stream backbone network.

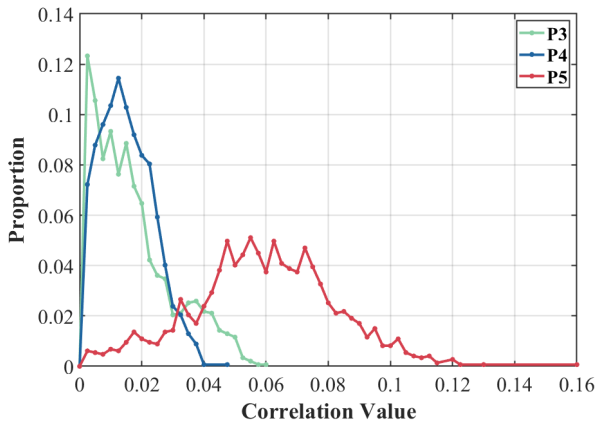


Figure 7: The amount of heterogeneous information (biases of data distributions between multimodal feature maps) in different levels of the network.

noise. LMA enhances the representation of homogeneous object features in each modality, while suppressing the extraction of heterogeneous noise to some extent. This makes the object information in the fusion features more significant.

**Ablation on the Adaptive Rank Allocation Strategy.** The baseline is a LMA detector with all adaptor matrices have evenly been set fixed rank to 6. Empirically, if there is a high degree of heterogeneity between two modalities, the data distribution of their feature maps will be biased. We thus utilize the multimodal data distribution biases to represent the amount of heterogeneous information. We extracted the features that would be fused in the three stages, P3, P4 and P5, of the two-stream baseline detector. And the data distribution biases between the multimodal feature

Table 4: Comparison of accuracy and parameters between LMA and two baselines in two ablation experiments on DroneVehicle val set.

Detectors	mAP@0.5	Params (M)	Param Increment
Two-stream Backbone	85.1	64.26	44.47%(19.78M)
LMA with fixed rank of 6	86.4	45.13	1.46%(0.65M)
<b>LMA</b>	<b>86.8</b>	<b>44.63</b>	<b>0.34%(0.15M)</b>

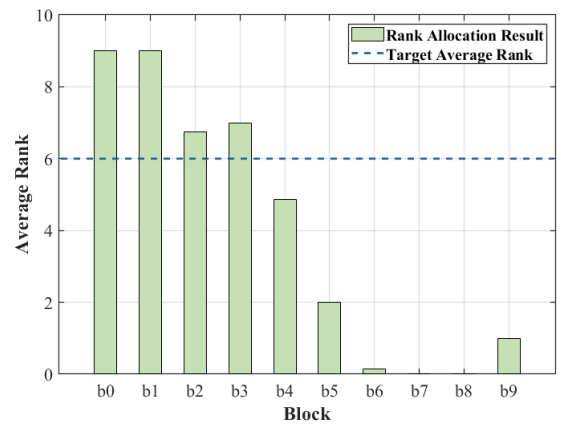


Figure 8: Rank allocation results (average rank of adaptors in each block within the backbone) after adaptive rank allocation. There are total 10 blocks in the backbone of YOLOv8l, denoted as 'b1' to 'b10' in data flow order.

maps of each stage are calculated separately. As shown in Figure 7, the data distribution bias is significantly lower in the P5 stage compared to the P3 stage. The experimental results demonstrate that shallow features contain more heterogeneous information than deep features in multimodal networks.

Figure 8 displays the average adaptor rank for each block in the backbone of the LMA following adaptive rank allocation strategy. As analyzed, LMA tends to allocate higher ranks to blocks of shallow levels such as 'b0', 'b1', 'b2' and 'b3', while allocating lower ranks to deep levels such as 'b6', 'b7', 'b8' and 'b9'. The lower-level blocks all have an average rank higher than the target rank, or even the same as the initial rank of the setup. In contrast, the higher-level blocks have smaller averages, some ('b7' and 'b8') even 0, indicating that the visible and infrared modalities share network parameters in these blocks. The experimental results in Table 4 demonstrate that the adaptive rank allocation strategy mitigates parameter redundancy, while improving the accuracy performance of the detector.



## 5 CONCLUSION

In this paper, we theoretically elaborate on the feature fusion process in multimodal two-stream backbone networks from the perspective of data distribution and point out their limitations. To solve this, we propose a novel multimodal detector integrated a shared backbone and lightweight modal adaptors, named LMA, to mitigate the distribution biases between homogeneous information. In addition, we design an adaptive rank allocation strategy to account for the varying heterogeneity in multimodal features across different levels. Extensive experiments are conducted on two multimodal detection datasets. We experimentally prove the large distribution biases and varying heterogeneity in multimodal features. The experimental results demonstrate that LMA achieves higher accuracy compared to two-stream backbone networks with minimal computation overhead. Specifically, on DroneVehicle val set, LMA achieves 10.4% accuracy improvement compared to the state-of-the-art method while achieving a 149M-parameters reduction. In the future, we plan to work on how to fuse heterogeneous information effectively with still little computation overhead, which we have not take into account in this paper.

## REFERENCES

- [1] Alexey Bochkovskiy, Chien-Yao Wang, and Hong-Yuan Mark Liao. 2020. Yolov4: Optimal speed and accuracy of object detection. *arXiv preprint arXiv:2004.10934* (2020).
- [2] Holger Caesar, Jasper Uijlings, and Vittorio Ferrari. 2018. Coco-stuff: Thing and stuff classes in context. In *Computer Vision and Pattern Recognition (CVPR)*. 1209–1218.
- [3] Jian-Feng Cai, Emmanuel J Candès, and Zuowei Shen. 2010. A singular value thresholding algorithm for matrix completion. *SIAM Journal on Optimization (SIOPT)* 20, 4 (2010), 1956–1982.
- [4] Zhaowei Cai and Nuno Vasconcelos. 2018. Cascade r-cnn: Delving into high quality object detection. In *Computer Vision and Pattern Recognition (CVPR)*. 6154–6162.
- [5] Nuo Chen, Jin Xie, Jing Nie, Jiale Cao, Zhuang Shao, and Yanwei Pang. 2023. Attentive alignment network for multispectral pedestrian detection. In *ACM International Conference on Multimedia (ACM MM)*. 3787–3795.
- [6] Qiang Chen, Yingming Wang, Tong Yang, Xiangyu Zhang, Jian Cheng, and Jian Sun. 2021. You only look one-level feature. In *Computer Vision and Pattern Recognition (CVPR)*. 13039–13048.
- [7] Zehui Chen, Chenhongyi Yang, Qiaofei Li, Feng Zhao, Zheng-Jun Zha, and Feng Wu. 2021. Disentangle your dense object detector. In *ACM International Conference on Multimedia (ACM MM)*. 4939–4948.
- [8] Xiyang Dai, Yinpeng Chen, Bin Xiao, Dongdong Chen, Mengchen Liu, Lu Yuan, and Lei Zhang. 2021. Dynamic head: Unifying object detection heads with attentions. In *Computer Vision and Pattern Recognition (CVPR)*. 7373–7382.
- [9] Xiyang Dai, Yinpeng Chen, Jianwei Yang, Pengchuan Zhang, Lu Yuan, and Lei Zhang. 2021. Dynamic detr: End-to-end object detection with dynamic attention. In *International Conference on Computer Vision (ICCV)*. 2988–2997.
- [10] Jian Ding, Nan Xue, Yang Long, Gui-Song Xia, and Qikai Lu. 2019. Learning RoI transformer for oriented object detection in aerial images. In *Computer Vision and Pattern Recognition (CVPR)*. 2849–2858.
- [11] Mark Everingham, SM Ali Eslami, Luc Van Gool, Christopher KI Williams, John Winn, and Andrew Zisserman. 2015. The pascal visual object classes challenge: A retrospective. *International Journal of Computer Vision (IJCV)* 111 (2015), 98–136.
- [12] Zheng Ge, Songtao Liu, Feng Wang, Zeming Li, and Jian Sun. 2021. Yolox: Exceeding yolo series in 2021. *arXiv preprint arXiv:2107.08430* (2021).
- [13] Ross Girshick. 2015. Fast r-cnn. In *International Conference on Computer Vision (ICCV)*. 1440–1448.
- [14] Jiaming Han, Jian Ding, Jie Li, and Gui-Song Xia. 2021. Align deep features for oriented object detection. *IEEE Transactions on Geoscience and Remote Sensing (TGRS)* 60 (2021), 1–11.
- [15] Xiao He, Chang Tang, Xin Zou, and Wei Zhang. 2023. Multispectral object detection via cross-modal conflict-aware learning. In *ACM International Conference on Multimedia (ACM MM)*. 1465–1474.
- [16] Edward J Hu, Yelong Shen, Phillip Wallis, Zeyuan Allen-Zhu, Yuanzhi Li, Shean Wang, Lu Wang, and Weizhu Chen. 2021. Lora: Low-rank adaptation of large language models. *arXiv preprint arXiv:2106.09685* (2021).
- [17] Z Huang, J Liu, L Li, K Zheng, and Z Zha. [n. d.]. Modality-adaptive mixup and invariant decomposition for RGB-Infrared person re-identification. *arXiv preprint arXiv:2203.01735* ([n. d.]).
- [18] Soonmin Hwang, Jaesik Park, Namil Kim, Yukyung Choi, and In So Kweon. 2015. Multispectral pedestrian detection: Benchmark dataset and baseline. In *Computer Vision and Pattern Recognition (CVPR)*. 1037–1045.
- [19] Stephanos Ioannou, Vittorio Gallese, and Arcangelo Merla. 2014. Thermal infrared imaging in psychophysiology: Potentialities and limits. *Psychophysiology* 51, 10 (2014), 951–963.
- [20] Xinyu Jia, Chuang Zhu, Minzhen Li, Wenqi Tang, and Wenli Zhou. 2021. LLVIP: A visible-infrared paired dataset for low-light vision. In *International Conference on Computer Vision (ICCV)*. 3496–3504.
- [21] Yingying Jiang, Xiangyu Zhu, Xiaobing Wang, Shuli Yang, Wei Li, Hua Wang, Pei Fu, and Zhenbo Luo. 2017. R2CNN: Rotational region CNN for orientation robust scene text detection. *arXiv preprint arXiv:1706.09579* (2017).
- [22] Glenn Jocher. 2020. YOLOv5 by Ultralytics. <https://doi.org/10.5281/zenodo.3908559>
- [23] Glenn Jocher, Ayush Chaurasia, and Jing Qiu. 2023. Ultralytics YOLO. <https://github.com/ultralytics/ultralytics>
- [24] Jiwon Kim, Hyeonjun Kim, Taejoo Kim, Namil Kim, and Yukyung Choi. 2021. MLPD: Multi-label pedestrian detector in multispectral domain. *IEEE Robotics and Automation Letters (RAL)* 6, 4 (2021), 7846–7853.
- [25] Vladimir Koltchinskii, Karim Lounici, and Alexandre B Tsybakov. 2011. Nuclear-norm penalization and optimal rates for noisy low-rank matrix completion. (2011).
- [26] Alex Krizhevsky, Ilya Sutskever, and Geoffrey E Hinton. 2017. ImageNet classification with deep convolutional neural networks. *Communications of the ACM (CACM)* 60, 6 (2017), 84–90.
- [27] Claudia Kuenzer and Stefan Dech. 2013. *Thermal infrared remote sensing: Sensors, methods, applications*. Vol. 17. Springer Science & Business Media.
- [28] Yann LeCun et al. 1989. Generalization and network design strategies. *Connectionism in Perspective (CP)* 19, 143-155 (1989), 18.
- [29] Chen Liang, Simiao Zuo, Minshuo Chen, Haoming Jiang, Xiaodong Liu, Pengcheng He, Tuo Zhao, and Weizhu Chen. 2021. Super tickets in pre-trained language models: From model compression to improving generalization. *arXiv preprint arXiv:2105.12002* (2021).
- [30] Tsung-Yi Lin, Priya Goyal, Ross Girshick, Kaiming He, and Piotr Dollár. 2017. Focal loss for dense object detection. In *International Conference on Computer Vision (ICCV)*. 2980–2988.
- [31] J Liu, S Zhang, S Wang, and DN Metaxas. [n. d.]. Multispectral deep neural networks for pedestrian detection. *arXiv preprint arXiv:1611.02644* ([n. d.]).
- [32] Jingjing Liu, Shaoting Zhang, Shu Wang, and Dimitris N Metaxas. 2016. Multispectral deep neural networks for pedestrian detection. *arXiv preprint arXiv:1611.02644* (2016).
- [33] Wei Liu, Dragomir Anguelov, Dumitru Erhan, Christian Szegedy, Scott Reed, Cheng-Yang Fu, and Alexander C Berg. 2016. Ssd: Single shot multibox detector. In *European Conference on Computer Vision (ECCV)*. Springer, 21–37.
- [34] Jianqi Ma, Weiyuan Shao, Hao Ye, Li Wang, Hong Wang, Yingbin Zheng, and Xiangyang Xue. 2018. Arbitrary-oriented scene text detection via rotation proposals. *IEEE Transactions on Multimedia (TMM)* 20, 11 (2018), 3111–3122.
- [35] Marco Manfredi and Yu Wang. 2020. Shift equivariance in object detection. In *European Conference on Computer Vision (ECCV)*. Springer, 32–45.
- [36] Q Ming, Z Zhou, L Miao, H Zhang, and L Li. [n. d.]. Dynamic anchor learning for arbitrary-oriented object detection. *arXiv preprint arXiv:2012.04150* ([n. d.]).
- [37] Pavlo Molchanov, Arun Mallya, Stephen Tyree, Iuri Frosio, and Jan Kautz. 2019. Importance estimation for neural network pruning. In *Computer Vision and Pattern Recognition (CVPR)*. 11264–11272.
- [38] Fang Qingyun, Han Dapeng, and Wang Zhaokui. 2021. Cross-modality fusion transformer for multispectral object detection. *arXiv preprint arXiv:2111.00273* (2021).
- [39] Fang Qingyun and Wang Zhaokui. 2022. Cross-modality attentive feature fusion for object detection in multispectral remote sensing imagery. *Pattern Recognition (PR)* 130 (2022), 108786.
- [40] Joseph Redmon, Santosh Divvala, Ross Girshick, and Ali Farhadi. 2016. You only look once: Unified, real-time object detection. In *Computer Vision and Pattern Recognition (CVPR)*. 779–788.
- [41] Joseph Redmon and Ali Farhadi. 2017. YOLO9000: Better, faster, stronger. In *Computer Vision and Pattern Recognition (CVPR)*. 7263–7271.
- [42] Joseph Redmon and Ali Farhadi. 2018. Yolov3: An incremental improvement. *arXiv preprint arXiv:1804.02767* (2018).
- [43] Shaoqing Ren, Kaiming He, Ross Girshick, and Jian Sun. 2016. Faster R-CNN: Towards real-time object detection with region proposal networks. *IEEE Transactions on Pattern Analysis and Machine Intelligence (TPAMI)* 39, 6 (2016), 1137–1149.
- [44] Victor Sanh, Thomas Wolf, and Alexander Rush. 2020. Movement pruning: Adaptive sparsity by fine-tuning. In *Neural Information Processing Systems (NeurIPS)*. 20378–20389.
- [45] Furong Shi, Tong Zhang, and Tao Zhang. 2020. Orientation-aware vehicle detection in aerial images via an anchor-free object detection approach. *IEEE Transactions on Geoscience and Remote Sensing (TGRS)* 59, 6 (2020), 5221–5233.
- [46] Yiming Sun, Bing Cao, Pengfei Zhu, and Qinghua Hu. 2022. Drone-based RGB-infrared cross-modality vehicle detection via uncertainty-aware learning. *IEEE Transactions on Circuits and Systems for Video Technology (TCSVT)* 32, 10 (2022), 6700–6713.
- [47] Ashish Vaswani, Noam Shazeer, Niki Parmar, Jakob Uszkoreit, Llion Jones, Aidan N Gomez, Łukasz Kaiser, and Illia Polosukhin. 2017. Attention is all you need. In *Neural Information Processing Systems (NeurIPS)*.
- [48] Xingxing Xie, Gong Cheng, Jiabao Wang, Xiwen Yao, and Junwei Han. 2021. Oriented R-CNN for object detection. In *International Conference on Computer Vision (ICCV)*. 3520–3529.
- [49] Maoxun Yuan, Yinyan Wang, and Xingxing Wei. 2022. Translation, scale and rotation: Cross-modal alignment meets RGB-infrared vehicle detection. In *European Conference on Computer Vision (ECCV)*. Springer, 509–525.
- [50] Maoxun Yuan and Xingxing Wei. 2024. C2Former: Calibrated and complementary transformer for RGB-Infrared object detection. *IEEE Transactions on Geoscience and Remote Sensing (TGRS)* (2024).
- [51] Heng Zhang, Elisa Fromont, Sébastien Lefevre, and Bruno Avignon. 2020. Multispectral fusion for object detection with cyclic fuse-and-refine blocks. In *International conference on image processing (ICIP)*. IEEE, 276–280.
- [52] Heng Zhang, Elisa Fromont, Sébastien Lefevre, and Bruno Avignon. 2021. Guided attentive feature fusion for multispectral pedestrian detection. In *Winter conference on Applications of Computer Vision (WACV)*. 72–80.
- [53] Lu Zhang, Zhiyong Liu, Xiangyu Zhu, Zhan Song, Xu Yang, Zhen Lei, and Hong Qiao. 2021. Weakly aligned feature fusion for multimodal object detection. *IEEE Transactions on Neural Networks and Learning Systems (TNNLS)* (2021).
- [54] Qingru Zhang, Minshuo Chen, Alexander Bukharin, Pengcheng He, Yu Cheng, Weizhu Chen, and Tuo Zhao. 2023. Adaptive budget allocation for parameter-efficient fine-tuning. In *International Conference on Learning Representations (ICLR)*.

- [55] Qingru Zhang, Simiao Zuo, Chen Liang, Alexander Bukharin, Pengcheng He, Weizhu Chen, and Tuo Zhao. 2022. Platon: Pruning large transformer models with upper confidence bound of weight importance. In *International Conference on Machine Learning (ICML)*. PMLR, 26809–26823.
- [56] Tianyi Zhao, Maoxun Yuan, and Xingxing Wei. 2024. Removal and Selection: Improving RGB-Infrared object detection via coarse-to-fine fusion. *arXiv preprint arXiv:2401.10731* (2024).
- [57] Bolei Zhou, Hang Zhao, Xavier Puig, Sanja Fidler, Adela Barriuso, and Antonio Torralba. 2017. Scene parsing through ade20k dataset. In *Computer Vision and Pattern Recognition (CVPR)*. 633–641.
- [58] Kailai Zhou, Linsen Chen, and Xun Cao. 2020. Improving multispectral pedestrian detection by addressing modality imbalance problems. In *European Conference on Computer Vision (ECCV)*. Springer, 787–803.
- [59] Wujie Zhou, Qinling Guo, Jingsheng Lei, Lu Yu, and Jenq-Neng Hwang. 2021. ECFNet: Effective and consistent feature fusion network for RGB-T salient object detection. *IEEE Transactions on Circuits and Systems for Video Technology (TCSVT)* 32, 3 (2021), 1224–1235.
- [60] Yixing Zhu, Jun Du, and Xueqing Wu. 2020. Adaptive period embedding for representing oriented objects in aerial images. *IEEE Transactions on Geoscience and Remote Sensing (TGRS)* 58, 10 (2020), 7247–7257.